

Regulating Diffusion Coefficient of Li⁺ by High Binding Energy Anion towards Ultra-Low Temperature Lithium-Ion Batteries

Qiu Chen,^[a] Pan Luo,^[a] Li Liao,^[a] Yin Shen,^[a] Xiaoshuang Luo,^[a] Xinpeng Li,^[a] Xuanzhong Wen,^[a] Jialin Song,^[a] Bo Yu,^[a] Junchen Chen,^[a] Bingshu Guo,^[a] Mingshan Wang,^{*[a]} Yun Huang,^[a] Fuliang Liu,^[b] Jiangtao Liu,^{*[b]} Zhen dong Li,^[c] Jingrun Ma,^[c] Shuiyong Wang,^{*[d]} and Xing Li^{*[a]}

Electrolyte design is the optimal strategy to achieve extremely low temperature operation of lithium-ion batteries. Here, the diffusion coefficient of Li⁺ is proposed to improve the ion transport kinetics at low temperatures. The diffusion coefficient of Li⁺ is improved by constructing a Li⁺ solvation sheath with weak steric effects. Specifically, high binding energy BF₄⁻ anions are added to a 1 M LiPF₆ in propyl acetate (PA) electrolyte. Since the binding energy of Li⁺ with BF₄⁻ is greater than that of PA. Therefore, the small-sized BF₄⁻ replaces the large-sized PA

molecule to form a Li⁺ solvation sheath with a weak steric effect, which increases the diffusion coefficient of Li⁺. Using the high diffusion coefficient electrolyte, the 800 mAh pouch cell retain 91% and 75% of its room temperature capacity at -40°C(0.5 C rate) and -60°C (0.2 C rate), respectively. And it also shows stable cycling at -40°C. This work provides a new strategy for designing low-temperature electrolytes of lithium-ion batteries.

Introduction

Since the commercial application of lithium-ion batteries (LIBs) in 1991, LIBs have stood out among rechargeable batteries with superior performance including large capacity, high voltage, excellent cycling performance and low self-discharge rate, thus, it has been considered as the most ideal and promising secondary batteries.^[1] However, the low temperature electrochemical performance of LIBs is limited due to several factors, including the rapidly increasing electrolyte viscosity, significantly lower ionic conductivity, slow interfacial charge transfer kinetics and Li⁺ transport in the electrodes.^[2] To overcome the limitations of low-temperature performance, various strategies

for low-temperature electrolytes have been reported. Among these strategies, many studies have focused on weakly solvating electrolytes due to the significant impact of Li⁺-desolvation on the low-temperature performance of LIBs.^[3] The strategy include the use of weakly solvating solvents and localized high-concentration electrolytes.^[4] Additionally, there are strategies such as using low polarity solvent electrolytes, co-intercalation electrolytes, and constructing solid electrolyte interphase (SEI) films.^[5]

The above studies have shown that LIBs can achieve operation at low temperatures through proper electrolyte engineering. However, it is noted that there are few reports on the improvement of Li⁺ diffusion processes in electrolyte at low temperature. Here, we explored the effect of diffusion coefficient of Li⁺ on the low temperature electrochemical performance of LIBs. The process of Li⁺ transporting (using discharge as an example) can be divided into five simple steps: 1) detachment of Li⁺ from the anode, 2) solvation of Li⁺, 3) movement of Li⁺ in the electrolyte (mass transfer), 4) desolvation of Li⁺, and 5) embedding of Li⁺ in the cathode. This work aims to optimize the third step, which involves two mass transfer processes: migration and diffusion. In batteries, the distance between the anode and cathode is relatively short, making the diffusion process the main component of this step. Therefore, enhancing the diffusion coefficient in this paper is equivalent to improving the kinetics of the mass transfer process, which in turn improves the ion transport kinetics. It is obvious that the diffusion of ions in a liquid becomes slow as the ion size increases. As the Li⁺ would be in the form of a solvation sheath in the electrolyte, the structure of the Li⁺ solvation sheath will affect the diffusion coefficient of Li⁺.^[6] Apparently, the largest size in the solvation sheath tends to be the solvent molecule.^[7] Therefore, it would

[a] Q. Chen, P. Luo, L. Liao, Y. Shen, X. Luo, X. Li, X. Wen, J. Song, Dr. B. Yu, Dr. J. Chen, Dr. B. Guo, Prof. M. Wang, Prof. Y. Huang, Prof. X. Li
School of New Energy and Materials
Southwest Petroleum University
Chengdu 610500 (China)
E-mail: ustbwangmingshan@163.com
lixing198141@yahoo.com

[b] F. Liu, Dr. J. Liu
State Key Laboratory of Advanced Chemical Power Sources
Guizhou Meiling Power Sources Co. Ltd.
Zunyi 563003 (China)
E-mail: ljt94070218@126.com

[c] Z. Li, J. Ma
Zhongbo Longhui Equipment Group Co., Ltd
Changxing 313100 (China)

[d] S. Wang
Suzhou Nuclear Power Research Institute Co., Ltd
Suzhou 215004 (China)
E-mail: wangshuiyong@foxmail.com

 Supporting information for this article is available on the WWW under
<https://doi.org/10.1002/batt.202400246>

be a favorable approach to use the method of reducing the solvent molecules in the solvation sheath to improve the diffusion coefficient of Li^+ . To exclude the effects of the addition of new solvents and changes in lithium salt concentration on the electrolyte, a mixture of a single solvent and lithium salts with different binding energies as the electrolyte was employed, where the lithium salts with high binding energy compete with solvent molecules for coordination with Li^+ . Importantly, the main focus of this paper is to investigate the effect of the physical properties of the electrolyte (diffusion coefficient) on the low temperature performance. Therefore, the battery systems studied try to avoid the influence of other factors, especially SEI. This is because electrolytes of different compositions will form SEI films of different compositions, and SEI films are critical to battery performance. Therefore, avoiding interference from SEI is the first requirement for studying diffusion coefficients. To prevent SEI interference, $\text{Li}_4\text{Ti}_5\text{O}_{12}$ (LTO) is selected as the anode of the battery. Compared with graphite or lithium metal anode, LTO also presents a higher potential, and the SEI, which is usually grown on the interface between the electrolyte and electrodes, is basically not formed on the surface of LTO. Therefore, the use of LTO as the anode eliminates any interference from SEI in the study of diffusion behavior. Therefore, the final experiment used LTO anode with LiCoO_2 (LCO) cathode with excellent low-temperature performance as the experimental system. LTO has the characteristic of spinel structure three-dimensional lithium ion diffusion channel, and has the advantages of excellent power characteristics and low temperature performance.^[8] Compared with graphite electrodes, LTO also presents a higher potential (1.55 V vs. Li^+/Li), and the SEI, which is usually grown on the interface between the electrolyte and the graphite electrodes, is basically not formed on the surface of LTO.^[5c,9] Therefore, when LTO is used as the anode, the requirements for the solvent's potential window and film-forming ability are reduced, while making the use of a single solvent possible.

Results and Discussion

Binding Energy of Different Components and Solvation Structure of Investigated Electrolytes

For low-temperature electrolytes, solvents need to fulfil the requirements of low melting point and low viscosity, such as linear carboxylates, ethers, nitriles, and sulfites (physical properties as shown in Table S1).^[4a,10] Through the filtering of pre-screening process, PA was used as the single solvent. To better represent the low-temperature performance of the design electrolyte, we chose a standard (STD) electrolyte (1 M LiPF_6 in EC/EMC = 3:7, by vol) for comparison. The pre-screening process excluded MA, EA, and BA due to their poor stability and low-temperature characteristics (Figure S 1). In the room temperature cycling test and the low-temperature discharge test, MA was found to have the lowest cycling stability among the four carboxylic acid esters and was lower than that of the STD electrolyte. Therefore, MA was excluded. In the subsequent

low-temperature cycling test, EA showed similar capacity to STD but better stability. BA had higher capacity than STD but similar stability. On the other hand, PA had a combination of higher capacity and stability. PA was used as the research subject in this experiment. And the binding energies of Li^+ with PA, PF_6^- and BF_4^- were -0.70 eV , -0.60 eV and -0.76 eV , respectively (Figure 1a). The binding energy of Li^+ with BF_4^- is greater than PA, so BF_4^- may replace PA in coordination with Li^+ . Herein, two electrolytes with PA as a single solvent was designed in this work, where the single-salt electrolyte of control group was 1 M LiPF_6/PA (denoted as SE), and the dual-salt electrolyte of treatment group was 0.7 M $\text{LiPF}_6 + 0.3 \text{ M LiBF}_4/\text{PA}$ (denoted as DE). Molecular dynamics simulations demonstrated that the introduction of LiBF_4 successfully replaced the PA without replacing the coordination of PF_6^- . The coordination numbers of PF_6^- and PA in the SE electrolyte (Figure 1b) are 2.30 and 2.61, respectively. The coordination numbers of PF_6^- , BF_4^- and PA in the DE electrolyte (Figure 1c) are 1.75, 0.93 and 2.17, respectively. Notably, the addition of BF_4^- significantly displaces the coordination of PA with Li^+ from 2.61 in SE to 2.17 in DE. Since the concentration of LiPF_6 changes from 1 M in SE to 0.7 M in DE, the coordination number of PF_6^- changes from 2.30 to 1.75. If scaled down in equal proportions by concentration, the coordination number of PF_6^- in DE is even higher than that in the SE electrolyte ($2.30 \times 0.7 = 1.61$). So the addition of BF_4^- did not affect the coordination of PF_6^- with Li^+ and even promoted it. The radial distribution function of the Li^+ with BF_4^- is significantly higher than PF_6^- and PA. This suggests that a large percentage of BF_4^- is involved in the solvation structure with Li^+ .

Snapshots (Figure 2a,b) from MD simulations manifest that BF_4^- in the DE electrolyte into the solvation structure. Most probable solvation structure of different electrolytes (Figure 2c) shows the surplus space left after PA coordination with Li^+ , so that PF_6^- , which has a smaller binding energy, can also be involved in the coordination through the interstitial space. Figure 2d shows that BF_4^- replaced the part of PA to form a new solvation structure, while reducing the volume of the whole structure. Therefore, it can be seen from Figure 2c,d,

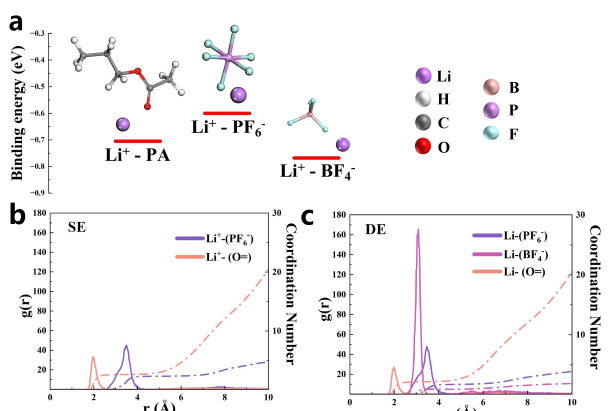


Figure 1. (a) The binding energy of Li^+ with PA, PF_6^- and BF_4^- ; radial distribution functions of the Li^+ with PA, PF_6^- and BF_4^- in the SE (b) and DE (c) electrolytes.

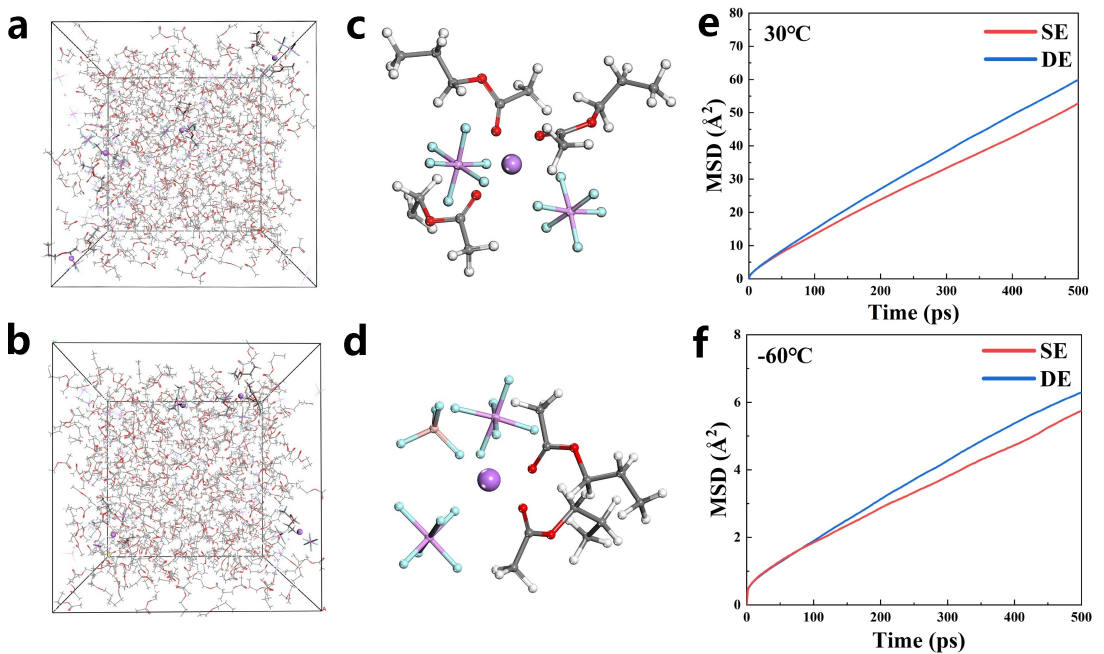


Figure 2. Snapshots of MD simulations of SE (a) and DE (b) electrolytes; Most probable solvation structure extracted from MD simulations of SE (c) and DE (d) electrolytes; MSD of the Li^+ at 30 °C (e) and -60 °C (f) electrolytes

there is still the surplus space after the coordination of Li^+ and PA molecules, allowing the low binding energy PF_6^- to participate in the coordination by entering the space. In the case of DE, the coordination involves the high binding energy BF_4^- replacing part of PA, which further widens the space. However, due to the limited amount of BF_4^- , there is still a space in the solvated structure. Therefore, the low binding energy PF_6^- can still participate in the coordination. The diffusion coefficients of Li^+ were determined by monitoring the mean-square displacement (MSD) over a 500 ps time interval, as illustrated in Figure 2e,f. The diffusion coefficient of Li^+ statistics can be found in Table S2. It can be found that the diffusion coefficient of Li^+ of the DE electrolyte is greater than that of the SE at both 30 °C and -60 °C. At -60 °C, the diffusion coefficient of Li^+ decreases significantly, to almost one-tenth of its value at 30 °C. It should be noted that the diffusion coefficient of Li^+ at -60 °C is $1.97 \times 10^{-7} \text{ cm}^2 \text{s}^{-1}$ of DE electrolyte and only $1.24 \times 10^{-7} \text{ cm}^2 \text{s}^{-1}$ of SE electrolyte. This indicates that the diffusion coefficient of Li^+ of the DE electrolyte will be higher at lower temperatures, resulting in faster low-temperature diffusion kinetics.

Physical Properties of Investigated Electrolytes

To further investigate the diffusion behavior of the electrolytes, we tested the self-diffusion coefficient of Li^+ by diffusion-ordered spectroscopy (DOSY).^[11] The ${}^7\text{Li}$ DOSY attenuation curves for lithium in the DE electrolyte is faster than for SE. (Figure 3a). The fitting results in self-diffusion coefficient of Li^+ in the SE electrolyte of $1.05 \times 10^{-6} \text{ cm}^2 \text{s}^{-1}$ compared to DE of $1.21 \times 10^{-6} \text{ cm}^2 \text{s}^{-1}$. It should be added that the diffusion

coefficients calculated by MD are applicable at the interface between the electrode and the electrolyte, since this is where changes in the Li^+ concentration occur. The self-diffusion coefficient, on the other hand, applies to the interior of the electrolyte, where the Li^+ concentration is more homogeneous. It can be seen that the diffusion rate of Li^+ in both DE electrolytes is higher than that in SE electrolyte. This indicates that addition of LiBF_4 successfully improved the diffusion coefficient of Li^+ in the electrolyte. Figure 3b-f shows the physical properties and photographs of different electrolytes at different temperatures. The ionic conductivity of the electrolyte at different temperatures was measured (Figure 3b), the ionic conductivity of SE electrolyte was 6.58 mS cm^{-1} at 20 °C, which is comparable to the STD electrolyte of commercial LIBs. Notably, the addition of LiBF_4 significantly reduced the conductivity, and the DE electrolyte conductivity was 4.77 mS cm^{-1} at 20 °C. However, at lower temperatures, the PA-based electrolyte exhibits less conductivity decay compared to the STD electrolyte. Below -20 °C, the conductivity of the PA-based electrolyte is higher than that of the STD electrolyte. At -60 °C, the SE and DE electrolytes have ionic conductivities of 0.76 mS cm^{-1} and 0.67 mS cm^{-1} , respectively, while the STD electrolyte has a conductivity of only 0.29 mS cm^{-1} . Figure 3c shows that the PA-based electrolyte has lower viscosity than the STD electrolyte, particularly at low temperatures. At -40 °C, the viscosities of the SE and DE electrolytes are 5.36 mPa s and 5.35 mPa s , respectively, while the STD electrolyte has a viscosity as high as 14.1 mPa s . The lower conductivity of LiBF_4 , which is consistent with previous studies,^[12] may be attributed to the stronger BF_4^- binding energy (Figure 1a). This binding energy limits the movement of Li^+ under the influence of an electric field. As a result the conductivity of the DE electrolyte is

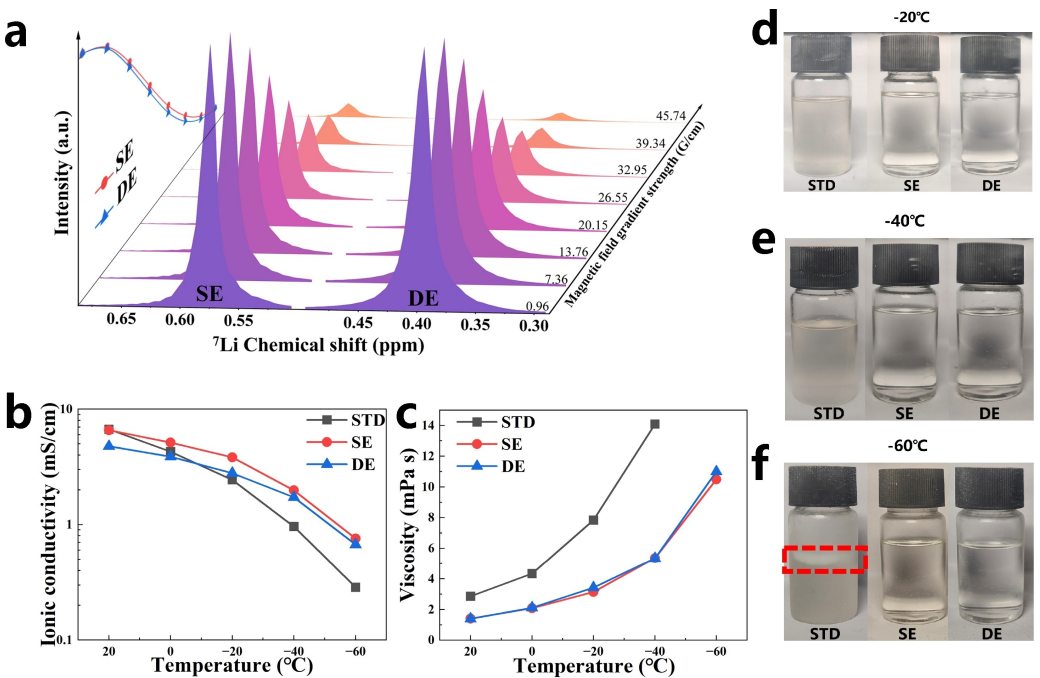


Figure 3. The characteristics of the electrolytes, a) ${}^7\text{Li}$ DOSY attenuation curves for lithium in SE and DE electrolyte. b) Measured ionic conductivity and c) viscosity of the investigated electrolytes at different temperatures; photographs of electrolytes at d) -20°C , e) -40°C , f) -60°C

reduced. Therefore, we chose a smaller concentration of LiBF_4 (0.3 M) as the DE electrolyte to avoid too large a difference in conductivity. It is also worth noting that the DE electrolyte with lower conductivity instead achieved superior low-temperature performance, which further proves the importance of the diffusion coefficient. The increase in viscosity may be due to the lower solubility of LiBF_4 compared to LiPF_6 . This causes the DE electrolyte to be more saturated relative to the SE electrolyte, resulting in a higher viscosity. The viscosity of the STD electrolyte exceeded the range as it partially solidified (Figure 3f) when the temperature was reduced to -60°C . The SE and DE electrolytes maintained a viscosity of 10.5 mPa s and 11 mPa s, respectively, at -60°C . To investigate the freezing point of the electrolyte, differential scanning calorimetry (Figure S2) measurement was conducted. The results indicate that the PA-based electrolyte has a freezing point of approximately 130°C . Furthermore, the STD electrolyte exhibited some heat absorption peaks between -40°C and -50°C , despite having a solidification point of -113°C . This observation is consistent with the partial solidification we observed. The electrolyte based on PA remains in a liquid state (Figure 3d-f) within the temperature range of -20 to -60°C . In addition to its high conductivity and viscosity, PA-based electrolytes also exhibit excellent wettability, with a contact angle of 28° with the PE separator, which is lower than the 38° observed in STD electrolytes (Figure S3).

Cycling Performance of LCO || LTO Coin Cells

To examine the electrochemical performance of the electrolytes, we conducted an experiment using coin cells. The study investigated the performance of various concentration ratios of double-salt electrolytes. The salt ratio was selected based on conductivity considerations. It is widely recognized that LiBF_4 has significantly lower conductivity than LiPF_6 . Therefore, excessive LiBF_4 content would greatly reduce the overall conductivity of the electrolyte, which would affect our assessment of the contribution of diffusive behavior. Meanwhile, we screened the electrochemical properties and found that higher LiBF_4 content decreases cycling stability (Figure 4). Therefore, we chose SE and DE component to test diffusion behavior. The results indicate that the stability of double-salt electrolytes decreases with increasing concentration ratio (Figure 4a). But the 0.7 M $\text{LiPF}_6 + 0.3$ M LiBF_4 in PA electrolyte shows the negligible attenuation; the discharge specific capacity at the 100th cycle was 149 mAh g^{-1} with 98% capacity retention. Pure LiPF_6 or LiBF_4 electrolytes exhibit the worst low-temperature discharge performance at -60°C , while the dual-salt electrolytes do not show a significant difference, maintaining a discharge specific capacity of about 80 mAh g^{-1} (Figure 4b). Based on these results, we selected SE and DE electrolytes for subsequent experiments. The initial coulombic efficiencies of PA-based electrolyte was notably higher than that of the STD electrolyte, reaching 96% (Figure S4a). The discharge capacities of the DE electrolyte at -40 and -60°C were 131 and 83 mAh g^{-1} , respectively (Figure S4b,d). These capacities were significantly higher than those of the SE electrolyte, which were 107 and 16 mAh g^{-1} . The STD electrolyte, however, has a

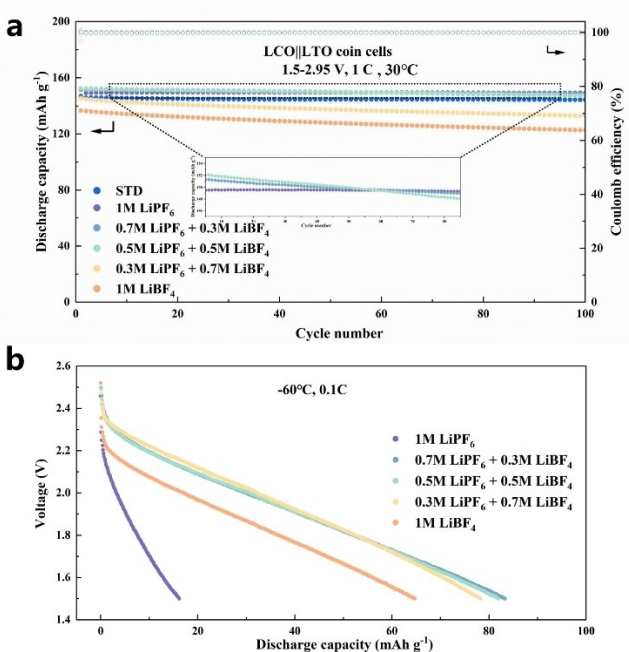


Figure 4. Cyclic performance at 30 °C (a) and discharge specific capacity at -60 °C (b) for LCO || LTO coin cells ($n/p = 1.05$) using PA-based electrolytes with different concentration ratios.

discharge capacity of only 43 mAh g⁻¹ at -40 °C and is unable to discharge at -50 °C. The DE electrolyte maintains excellent rate performance, even achieving the 5 C discharge capacity of 72 mAh g⁻¹ at room temperature, which is significantly higher than the 38 and 9 mAh g⁻¹ of the SE and STD electrolytes (Figure S4e).

Cycling Performance of LCO || LTO Pouch Cells

To verify the practicality of low-temperature electrolytes, we prepared 800 mAh pouch cells (Figure S5). After 350 cycles of DE electrolyte with the rate of 1 C, the LCO || LTO pouch cell displayed a capacity of 710 mAh with 98% capacity retention (Figure S6), which is slightly higher than SE (682 mAh, 97%). To further investigate the effect of diffusion coefficient of Li⁺ on the low temperature performance of the electrolyte, both low temperature discharge and low temperature charge/discharge tests were performed. It is easy to see from Figure 5a,b that the high diffusion coefficient DE electrolyte presents significantly lower voltage polarization as well as higher discharge capacity at different low temperature discharge. The advantage increases as the temperature decreases. Even under -60 °C with the rate of 0.2 C, it still achieves a discharge capacity of 536 mAh, corresponding to a 75% capacity retention of 30 °C. Comparatively, the SE electrolyte is only 281 mAh with 40% capacity retention of 30 °C. Similarly, the DE electrolyte has a slightly higher low-temperature charge capacity than the SE electrolyte and exhibits a lower voltage polarization (Figure 5c,d). The pouch cell also showed stable low temperature cycle performance of 515 mAh at -40 °C with the rate of 0.2 C

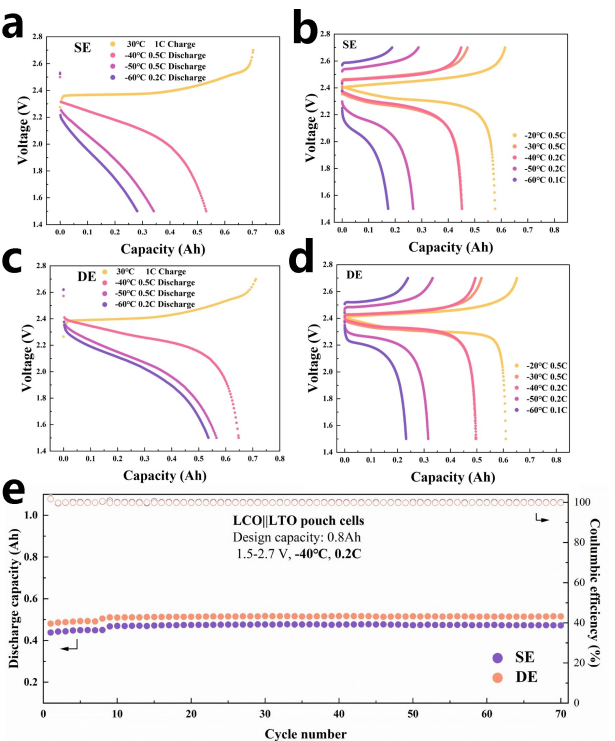


Figure 5. Discharge profiles of SE (a) and DE (b) electrolytes at different temperatures, charge/discharge profiles of SE (c) and DE (d) electrolytes at different temperatures; (e) cycle performance of pouch cells at -40 °C.

(Figure 5e). For the rate test at a low temperatures of -20 °C, the DE electrolyte maintains a capacity of 298 mAh with the rate of 2 C (Figure S7). As explained in the response to the mass transfer process involves both migration and diffusion. The voltage at the positive and negative electrodes increases as the charging and discharging rate increases. The migration process is driven by the electric field, enhancing the contribution of migration to the mass transfer process at large rate. Conductivity reflects the rate of ion migration to some extent. Therefore, the SE electrolyte, which has a higher conductivity, has a narrower rate gap with the DE electrolyte for mass transfer at large multiplication rates. In low temperature environments, the situation described above is applicable. However, at room temperature, the migration rates of both SE and DE electrolytes are enhanced similarly with an increase in rate. As a result, the rate performance of room temperature of both DE electrolytes is significantly better than that of the SE electrolyte, as shown in Figure S4e. The above results show that at ultra-low temperatures, electrolytes with high diffusion coefficients can still achieve faster kinetics due to rapid diffusion for better low-temperature performance.

High Temperature Testing and Graphite Cell Testing

To explore the wide temperature applicability of PA-based electrolytes, coin cells were assembled to test the high-temperature performance. Figure S8 shows that the DE electrolyte

remains stable at 60 °C. After 50 cycles of DE electrolyte at a rate of 1 C, the LCO || LTO coin cell displayed a capacity of 140 mAh g⁻¹ with 86% capacity retention, indicating its potential for use at a wide range of temperatures. The above tests demonstrate the excellent performance of DE electrolyte in LCO || LTO battery system. To further evaluate the applicability of the DE electrolyte, we assembled coin cells to test the LCO || graphite battery system. It is important to note that the PA-based electrolyte does not contain a film-forming component. Therefore, the graphite electrodes were activated using STD electrolyte. And the activated graphite electrodes was paired with DE electrolyte for testing. Figure S9 shows that at a high cutoff voltage of 4.45 V, the DE electrolyte had a discharge capacity of 95 mAh g⁻¹ at the 80th cycle with a capacity retention of 67%. This suggests that the DE electrolyte can be used in the graphite system with an appropriate improvement strategy. Furthermore, the LCO || graphite coin cell with DE electrolyte maintains a discharge specific capacity of 142 mAh g⁻¹ at -40 °C, with a capacity retention of 80% of the room temperature (Figure S10).

The low-temperature electrolytes reported in recent literature are summarized and are compared with this DE, shown in Table S3. The results demonstrate that the pouch cell prepared with DE in our work achieves exceptional low-temperature performance due to the employed strategy to increase the diffusion coefficient.

Conclusions

This work aims to optimize the mass transfer step, which involves two processes: migration and diffusion. In batteries, the distance between the anode and cathode is relatively short, making the diffusion process the main component of this step. Therefore, enhancing the diffusion coefficient is equivalent to improving the kinetics of the mass transfer process, which in turn improves the ion transport kinetics.

In summary, a high diffusion coefficient of Li⁺ electrolyte has been rationally designed by introducing the high binding energy BF₄⁻ anion. Theoretical calculations and spectroscopic characterization indicate that the BF₄⁻ anion replaces the solvent molecule without affecting the coordination of the PF₆⁻. The newly formed solvation sheath shows a weak steric effect, which significantly increases the diffusion coefficient of Li⁺. Benefiting from a high diffusion coefficient of Li⁺, the pouch cell retain 91% of capacity at -40 °C(0.5 C rate) and 75% of capacity at -60 °C (0.2 C rate) and show stable cycling at -40 °C. This work demonstrates the effect of the diffusion coefficient of Li⁺ on low temperature LIBs and provides a new approach to the design of low temperature electrolytes.

Experimental Section

Electrolyte Preparation

The commercial electrolyte (denoted as the standard electrolyte, STD) consisting of 1.0 M LiPF₆ in a mixture of ethylene carbonate (EC) and ethyl methyl carbonate (EMC) (3:7 by volume ratio) was purchased from Guangdong Canrd New EnergyTechnology Co., Ltd. The propyl acetate (PA) were purchased from Aladdin Chemical Reagent Network. Lithium Hexafluorophosphate (LiPF₆) were purchased from Xiamen Shouneng Technology Co., Ltd. Lithium Tetrafluoroborate (LiBF₄) were purchased from Beike (Shenzhen) Energy Technology Co., Ltd. LiPF₆ is added to PA solvent to make an electrolyte with a concentration of 1.0 M (denoted as the single-salt electrolyte, SE). As an improved electrolyte, 0.3 M LiPF₆ was replaced with LiBF₄ to obtain 0.7 M LiPF₆ and 0.3 M LiBF₄ double salt electrolytes (denoted as the dual-salt electrolyte, DE). The preparation and storage of the above electrolyte are carried out in an Ar-filled glove box (Dellix industry Co., Ltd.) with H₂O contents less than 0.1 ppm and O₂ contents less than 1 ppm.

Preparation of Electrode Sheet and Battery

For different cells, electrodes produced by different companies were used in this experiment. The CR2032 coin cell uses electrodes produced by Guangdong Canrd New EnergyTechnology Co., Ltd. The active material content of commercial LiCoO₂ (LCO) film cathode is 96.5%, the loading capacity of cathode active material was 8.3 mg cm⁻² (1.47 mAh cm⁻²). The active material content of commercial Li₄Ti₅O₁₂ (LTO) anode film is 90.0%, the loading capacity of anode active material was 11.5 mg cm⁻² (1.55 mAh cm⁻²). The active material content of commercial graphite anode film is 95.7%, the loading capacity of anode active material was 5.55 mg cm⁻² (1.89 mAh cm⁻²). The pouch cell uses electrodes produced by Zhongbo Longhui (Changxing) Information technology Co., Ltd. The active material content of commercial LiCoO₂ (LCO) film cathode is 94.0%, the loading capacity of cathode active material was 10.9 mg cm⁻² (1.54 mAh cm⁻²). The active material content of commercial Li₄Ti₅O₁₂ (LTO) film anode is 93.0%, the loading capacity of anode active material was 8.8 mg cm⁻² (1.39 mAh cm⁻²). The preparation cells assembly were performed inside an Ar-filled glove box. The pouch cells were prepared by the laminated pouch cell equipment (Kejing, MSK-111 A-ES).

Characterization and Electrochemical Tests

The self-diffusion coefficient was measured by a pulsed-gradient spin-echo nuclear magnetic resonance (PGSE-NMR) method using a Bruker Avance III HD. The spectra of lithium cation was measured using ⁷Li atoms. The attenuation of the echo signal *E* was obtained by varying the duration δ of the pulsed-field gradient multiprobe at a fixed amplitude *g*. *D* was determined by the regression of the Stejskal-Tanner equation:^[13]

$$E = \exp[-\gamma^2 \delta^2 g^2 D(\Delta - \frac{\delta}{3})] \quad (1)$$

where γ is the gyromagnetic ratio of the observed nuclei and is the interval between diffusion measurements. *D* is independent of Δ for the homogeneous samples. The viscosity of these electrolytes was tested using a rotary viscometer (Jingtian, NDJ-8S). The contact angle data was tested on the contact angle tester (Dataphysics, OCA25) at 25 °C. The melting point of the electrolyte were analyzed by differential scanning calorimeter (Netzsch, DSC 404 F1/F3 Pegasus). Ionic conductivity was measured by electrochemical

impedance spectroscopy (EIS) in the temperature range from -60 to 20°C with the frequency from 1 to 10^5 Hz on an electrochemical working station (CHI760E). All the electrolyte was sandwiched between two stainless steel electrodes for the ionic conductivity test. The ionic conductivity σ was calculated from:

$$\sigma = \frac{L}{S \cdot R} \quad (2)$$

where L is the thickness of the separator; S is the area of stainless steel; and R is the bulk resistance. And the galvanostatic test data was obtained on the Neware test system at room temperature and on the Land BT2000 test system at low temperature, respectively.

Computational Details

All the calculations based on density functional theory (DFT) were carried out in Gaussian software package. Geometric optimization and frequency calculations were performed at B3LYP/6-311+G(d,p) level. The PA dielectric constant (6.00) acted as the SMD (Solvation Model Based on Density)^[14] was used to study the effect of environment. The binding energy (E_b) between two components was obtained as follows:

$$E_b = E(\text{Li}^+\text{-A}) - E(\text{Li}^+) - E(\text{A}) \quad (3)$$

where $E(\text{Li}^+\text{-A})$, $E(\text{Li}^+)$ and $E(\text{A})$ are the total energies of the $\text{Li}^+\text{-A}$ complexes, Li-ion and A component, respectively. A represents anionic or solvents. Molecular dynamics (MD) simulations were performed using the Materials Studio Force module. Molecules and ions including PA, PF_6^- , BF_4^- , and Li^+ were built and got geometry optimization through Dmol³ software. Two electrolytes was built by Amorphous Cell module. The number of molecules ratio in the SE electrolyte: LiPF_6 : PA = 50:420; The number of molecules ratio in the DE electrolyte: LiPF_6 : LiBF_4 : PA = 35:15:420; The COMPASSIII force field^[15] was adopted for all molecules and ions. Pre-equilibrium calculations for electrolytes were performed using the NPT ensemble at 213 K and 303 K for a period of 200 ps each. Subsequently, the NVT ensemble was employed to achieve a final equilibrated state for electrolytes at 213 K and 303 K over a period of 2000 ps each. Finally, the radial distribution function (RDF) and coordination numbers ($n(r)$) analyses were conducted on the last 1 ns of the NVT production steps. The mean-squared displacement (MSD) was tracked over the last 500 ps to exclude short time regions when molecules are confined. The diffusion coefficient can be represented by tracking the mean squared displacement (MSD) as:^[4c]

$$D = \frac{1}{6Na} \lim_{t \rightarrow \infty} \frac{d}{dt} \sum_{i=1}^{Na} \langle [ri(t) - ri(0)]^2 \rangle = \frac{1}{6} \lim_{t \rightarrow \infty} \frac{d}{dt} \text{MSD} \quad (4)$$

in which $ri(t)$ and $ri(0)$ is the position of atom i at time t and time 0 .

Supporting Information

The authors have cited additional references within the Supporting Information.^[16,17]

Acknowledgements

This work was supported by the National Natural Science Foundation of China (grant No. 52072322), and the Department of Science and Technology of Sichuan Province (CN) (grant no. 23GJHZ0147, 23ZDYF0262, 2022YFG0294, 2019-GH02-00052-HZ).

Conflict of Interests

The authors declare no conflict of interest.

Data Availability Statement

The data that support the findings of this study are available from the corresponding author upon reasonable request.

Keywords: diffusion coefficient • lithium-ion batteries • low temperature • steric effect

- [1] a) M. Armand, J.-M. Tarascon, *Nature* **2008**, *451*, 652; b) D. Di Lecce, R. Verrelli, J. Hassoun, *Green Chem.* **2017**, *19*, 3442; c) A. Varzi, K. Thanner, R. Scipioni, D. Di Lecce, J. Hassoun, S. Dörfler, H. Altheus, S. Kaskel, C. Prehal, S. A. Freunberger, *J. Power Sources* **2020**, *480*, 228803; d) A. A. Kebede, T. Coosemans, M. Messagie, T. Jemal, H. A. Behabtu, J. Van Mierlo, M. Berecibar, *J. Energy Storage* **2021**, *40*, 102748.
- [2] a) S. Zhang, K. Xu, T. Jow, *J. Power Sources* **2003**, *115*, 137; b) M. Smart, B. Ratnakumar, K. Chin, L. Whittanack, *J. Electrochem. Soc.* **2010**, *157*, A1361; c) K. Xu, *J. Electrochem. Soc.* **2009**, *156*, A751.
- [3] a) Q. Li, D. Lu, J. Zheng, S. Jiao, L. Luo, C.-M. Wang, K. Xu, J.-G. Zhang, W. Xu, *ACS Appl. Mater. Interfaces* **2017**, *9*, 42761; b) Y. Zou, F. Cheng, Y. Lu, Y. Xu, C. Fang, J. Han, *Small* **2023**, *19*, 14.
- [4] a) J. Holoubek, H. Liu, Z. Wu, Y. Yin, X. Xing, G. Cai, S. Yu, H. Zhou, T. A. Pascal, Z. Chen, *Nat. Energy* **2021**, *6*, 303; b) T. Ma, Y. Ni, Q. Wang, W. Zhang, S. Jin, S. Zheng, X. Yang, Y. Hou, Z. Tao, J. Chen, *Angew. Chem.* **2022**, *134*, e202207927; c) X. Dong, Y. Lin, P. Li, Y. Ma, J. Huang, D. Bin, Y. Wang, Y. Qi, Y. Xia, *Angew. Chem. Int. Ed.* **2019**, *58*, 5623; d) J. Holoubek, K. Kim, Y. Yin, Z. Wu, H. Liu, M. Li, A. Chen, H. Gao, G. Cai, T. A. Pascal, P. Liu, Z. Chen, *Energy Environ. Sci.* **2022**, *15*, 1647; e) W. Lin, J. Li, J. Wang, K. Gu, H. Li, Z. Xu, K. Wang, F. Wang, M. Zhu, Y. Fan, H. Wang, G. Tao, N. Liu, M. Ding, S. Chen, J. Wu, Y. Tang, *Small* **2023**, *19*, 2207093
- [5] a) B. Nan, L. Chen, N. D. Rodrigo, O. Borodin, N. Piao, J. Xia, T. Pollard, S. Hou, J. Zhang, X. Ji, *Angew. Chem. Int. Ed.* **2022**, *61*, e202205967; b) Y. Yang, Y. Chen, L. Tan, J. Zhang, N. Li, X. Ji, Y. Zhu, *Angew. Chem. Int. Ed.* **2022**, *61*, e202209619; c) D.-J. Yoo, Q. Liu, O. Cohen, M. Kim, K. A. Persson, Z. Zhang, *ACS Appl. Mater. Interfaces* **2022**, *14*, 11910; d) X. Shangguan, G. Xu, Z. Cui, Q. Wang, X. Du, K. Chen, S. Huang, G. Jia, F. Li, X. Wang, D. Lu, S. Dong, G. Cui, *Small* **2019**, *15*, 1900269; e) R. Han, Z. Wang, D. Huang, F. Zhang, A. Pan, H. Song, Y. Wei, Y. Liu, L. Wang, Y. Li, J. Xu, J. Hu, X. Wu, *Small* **2023**.
- [6] C.-C. Su, M. He, R. Amine, Z. Chen, K. Amine, *J. Phys. Chem. Lett.* **2018**, *9*, 3714.
- [7] D. Lu, R. Li, M. M. Rahman, P. Yu, L. Lv, S. Yang, Y. Huang, C. Sun, S. Zhang, H. Zhang, J. Zhang, X. Xiao, T. Deng, L. Fan, L. Chen, J. Wang, E. Hu, C. Wang, X. Fan, *Nature* **2024**.
- [8] J. M. Feckl, K. Fominykh, M. Döblinger, D. Fattakhova-Rohlfing, T. Bein, *Angew. Chem.* **2012**, *124*, 7577.
- [9] I. Belharouak, Y.-K. Sun, W. Lu, K. Amine, *J. Electrochem. Soc.* **2007**, *154*, A1083.
- [10] a) C. Zhu, W. Lv, J. Chen, C. Ou, Q. Zhang, H. Fu, H. Wang, L. Wu, S. Zhong, *J. Power Sources* **2020**, *476*, 228697; b) S. Lei, Z. Zeng, M. Liu, H. Zhang, S. Cheng, J. Xie, *Nano Energy* **2022**, *98*, 107265; c) Y. Zhao, Z. Hu, Z. Zhao, X. Chen, S. Zhang, J. Gao, J. Luo, *J. Am. Chem. Soc.* **2023**, *145*, 22184.

- [11] Y. Cohen, L. Avram, L. Frish, *Angew. Chem. Int. Ed.* **2005**, *44*, 520.
- [12] S. Hwang, D.-H. Kim, J. H. Shin, J. E. Jang, K. H. Ahn, C. Lee, H. Lee, *J. Phys. Chem. C* **2018**, *122*, 19438.
- [13] E. Stejskal, *J. Chem. Phys.* **1965**, *43*, 3597.
- [14] A. V. Marenich, C. J. Cramer, D. G. Truhlar, *J. Phys. Chem. B* **2009**, *113*, 6378.
- [15] a) H. Sun, *J. Phys. Chem. B* **1998**, *102*, 7338; b) H. Sun, Z. Jin, C. Yang, R. L. Akkermans, S. H. Robertson, N. A. Spenley, S. Miller, S. M. Todd, *J. Mol. Model.* **2016**, *22*, 1.
- [16] S. Yuan, S. Cao, X. Chen, J. Wei, Z. Lv, H. Xia, J. Li, H. Zhang, L. Liu, C. Tian, L. Chen, W. Zhang, Z. Xing, H. Li, S. Li, Q. Zhu, X. Feng, X. Chen, *Advanced Materials* **2024**, *36*, 2311327.
- [17] Y. Yang, Z. Fang, Y. Yin, Y. Cao, Y. Wang, X. Dong, Y. Xia, *Angew. Chem. Int. Ed.* **2022**, *61*, e202208345.

Manuscript received: April 16, 2024
Accepted manuscript online: April 18, 2024
Version of record online: May 29, 2024
